Thermal and Mechanical Testing and Modeling at Extreme Temperatures, Strains or Strain Rates

Viktor Gonda

Óbuda University

Doctoral School of Materials Sciences and Technologies

Thermal and Mechanical Testing and Modeling at Extreme Temperatures, Strains or Strain Rates

Habilitation thesis

Viktor Gonda, PhD

Department of Materials Technologies

Bánki Faculty of Mechanical and Safety Engineering

Óbuda University

Budapest, Hungary

2022

Contents

I Introduction

Deformation and thermal behavior of materials in materials technologies particularly in microelectronic technologies, metallurgical technologies and mechanical technologies determine the foundation for analysis and development of new engineering applications. Fundamental state variables for materials technologies involving thermal and deformation processes are temperature and strain, as well as their rate functions, i.e. heating/cooling rate and strain rate. Material behavior at the extremes of these variables are of great interest in extending boundaries of the technologies.

Rapid thermal annealing was developed for microelectronic technologies to shorten thermal cycles and restrain diffusion while activating dopants in silicon. An extreme short transient thermal cycle is inherent with surface melt laser treatments with nanosecond pulses, which provide ultimately rapid localized heat treatments with further application possibilities for thermal restricted structures and for ultrashallow junctions. For activation of implanted dopants in bulk silicon with excimer laser annealing, the optimal laser energy density depends on the substrate heating, the pulse width and shape besides the structural layout of the irradiated device structure. These parameters determine the thermal cycle and the heat affected zone. In the melted and regrown surface region of silicon, very high dopant activation can be achieved with perfect crystalline quality, however beyond the shallow heat affected zone, implantation damage would not be annihilated. The work presented in Chapter 1 provides an approach for tailoring the thermal budget for rapid thermal annealing of low energy implants with XeCl excimer laser setups: either a long pulse single laser setup, or a double laser setup with 25 ns native pulse width was used. In the latter, the pulse shape and the temporal thermal profile can be tailored with short pulse offsets.

Materials technologies at the near melting point of the materials besides special heat treatments are primary metallurgical technologies. Along the metallurgical length in continuous casting, the temperature within the steel strand ranges from above melt temperature down to sub-solidus during the cooling. In this range, particularly in the mushy zone, mechanical properties drastically drop at above the critical temperatures as zero deformation temperature and the zero strength temperature due to the presence of liquid phase. These critical temperatures depend on local chemical and microstructural properties. The work in Chapter 2 demonstrates the variations of critical temperatures across the continuous cast strand. By taking samples from the as-cast ST52-3 steel strand from positions of the columnar grains zone and from the segregated zone located at the centerline of the strand, the effect of variations in chemical compositions was investigated by high temperature tensile testing on hot strength and ductility parameters. Samples were also taken from a hot rolled sheet with finer microstructure for a reference. A significant drop in zero ductility temperature was found due to segregations in the centerline compared to the columnar zone within the strand.

High strain rate extremes occur at special forming technologies as electromagnetic forming, where deformations are completed within a fraction of a second. Controlled discharging of capacitor banks provide power to an electromagnet, in which a sufficiently high electromagnetic force is generated to be applied for metal forming. A frequent industrial application of electromagnetic forming is joining by electromagnetic compression of tubular parts. The goodness of the joints is determined by the strength of the joint, and it is considered excellent if it reaches the strength of the weaker material. Modeling of the processing is twofold: coupled electromagnetic and mechanical modeling of the electromagnetic forming requires large computational resources, where electromagnetic part has much higher computation costs than the mechanical calculations. Subsequently, mechanical modeling of joint strength reveals (in)sufficient deformations originated from the joining stage. In Chapter 3, joining of tubular parts are demonstrated by using radial and axial grooves to employ interlocking by form fitting. Furthermore, a computational cost effective modeling is developed with uncoupled mechanical modeling of the electromagnetic forming by calculating the applied forming pressure with an equivalent circuit model; and subsequently modeling the tensile testing to evaluate the goodness of the joint.

Severe plastic deformation technologies provide high extremes of strain magnitude with the purpose of altering mechanical properties. Large amount of strengthening can be achieved by equal channel angular pressing (ECAP) without the modification of the cross section of the semi-product. For pure metals, this high strength is accompanied with low thermal stability due to the uninhibited driving force for recrystallization by the large stored energy. Besides the strain hardening, grain refinement contributes to the overall strengthening of the material in ECAP processing. The applied deformation is determined by the geometry of the extrusion die and the number of passes, nevertheless the microstructural changes and the stored energies are also dependent on the processing routes as well as on the processing temperature. Due to the large applied deformation, the stored energy is high, therefore the driving force for recrystallization is high, resulting in low thermal stability. For this reason, thermal stability of pure metals processed by ECAP are extensively studied. In the work presented in Chapter 4, the chosen technological route was elevated temperature single pass ECAP processing of copper and its effect on the thermal behavior during the restoration processes of the processed samples was studied.

Common processes for additive manufacturing technology for metal components are laser heating/melting processes, such as selective laser melting. In this process, a metal powder layer is applied to the heated surface of the base plate of same material quality, and the corresponding layer of the model geometry is irradiated to melting by a laser. It continues layer-to-layer until the part is completely built. During the process, different thermal loads are exposed to different parts of the workpiece, resulting in a distribution of inhomogeneous residual stresses over the piece, causing warpage. Simulations of additive manufacturing processes require high computational power, therefore simplifications and assumptions are established about modeling. Related to the geometry, meso/macro scale simulations are considered for the simulations of the printing process, and from a physical point of view, it is possible to use solely a mechanical model to estimate the deformations within a relatively short computational time. The key to the physical simplification is the application of inherent strains, which can be considered as a calibration parameter for a specific material quality, machine, and process parameter set. In the computational study presented in Chapter 5, the effect of the magnitude of inherent strain is examined for the simulated deformations of a printed specimen, where the material grade is either of MS1 or 316L steel powders. While the same sets of inherent strain values with different magnitude and directional variations are chosen, allowing isotropic and orthotropic behavior too, the resulting deformation in the printed part may also be strongly influenced by the elastic/plastic mechanical properties of the different steel grades.

II Original Contributions

1 Thermal budget considerations for rapid thermal annealing [1]

Ultrashallow junctions below 50 nm with excellent electrical properties can be formed for advanced microelectronic devices by excimer laser annealing of implanted dopants. In the melted and regrown surface region of silicon, very high dopant activation can be achieved with perfect crystalline quality. The heat affected zone is very small, which makes this method applicable for device structures with thermal limitations; and the thermal cycle is very short, therefore diffusion will not occur in the solid. This technology was integrated into the laboratory fabrication line [Gonda, 2008], and further evolution of the technique was shown in [2][3][4]. Applications were shown in conjunction with silicon-on-glass bipolar transistors [Lorito et al., 2006], SiGe HBT [Lorito et al., 2008], and high-k metal gate MISFET [3], and devices with double sided contacts [4].

However, due to the extremely low thermal budget, significant implantation damage may remain below the melted and regrown region [Gonda et al., 2006] at a critical depth about 100 nm for the low energy implants. Therefore, for some applications an increased thermal budget would be beneficial with tailored temporal and spatial thermal profiles to reduce residual damage.

For activation of implanted dopants in bulk silicon with excimer laser annealing, the optimal laser energy density depends on the substrate heating, the pulse width and shape besides the structural layout of the irradiated device structure. These parameters determine the thermal cycle and the heat affected zone. In this work, tailoring the thermal budget is evaluated for rapid thermal annealing of low energy implants with XeCl excimer laser setups: either a long pulse (180 ns) single laser setup, or a double laser setup with 25 ns native pulse width was used. In the latter, the pulse shape and the temporal thermal profile can be tailored with short pulse offsets. This way the total thermal budget can be increased while the laser energy of each pulse is decreased, for the same sheet resistance. The two methods are compared by sheet resistance measurements on laser annealed arsenic implants. The temporal and spatial thermal profiles were also calculated for both methods. Results show that the laser energy density can range from 600-1850 mJ/cm^2 to give full activation with different thermal profiles based upon the method used.

1.1 Experimental and modeling procedures

A double laser system and a long pulse laser system were used in the experiments. The former consists of two Lambda Physics XeCl laser sources emitting at 308 nm wavelength with a native pulse width of 25 ns measured at full width at half maximum (FWHM). The lasers can be ignited with pre-defined delays (pulse offsets) by the pulse generator in the typical range from 0 ns to 400 ns. When 0 offset is used, then the two lasers are simultaneously ignited, however a time jitter can occur, which is about 4 ns at 1σ. The second laser system is a special long pulse XeCl system built by Excico, where the pulse width is 180 ns FWHM. The temporal pulse shapes for the double laser system with 0 and 100 ns offset are shown in Figure 1.1, together with the shape of long laser pulse. Both setups consist of spatial spot shaping for top hat intensity profiles. The samples were 4” diameter, 0.5 mm thick p-type silicon wafers implanted with As^{+} at 15 keV with a dose of 5 x 10^{14} cm^{-2}. Four laser annealing recipes were defined:

a) substrate heated to 300°C, 25 ns pulse,

b) room temperature substrate with 25 ns pulse,

c) room temperature substrate, double pulsed 2 x 25 ns pulse with 100 ns delay, and

d) room temperature substrate with a single 180 ns pulse.

The processing was executed in vacuum, and laser fluences were set on columnar paths over the wafers in the range from 500-3000 mJ/cm^2. Subsequently, the sheet resistance was measured with 4-point probe.

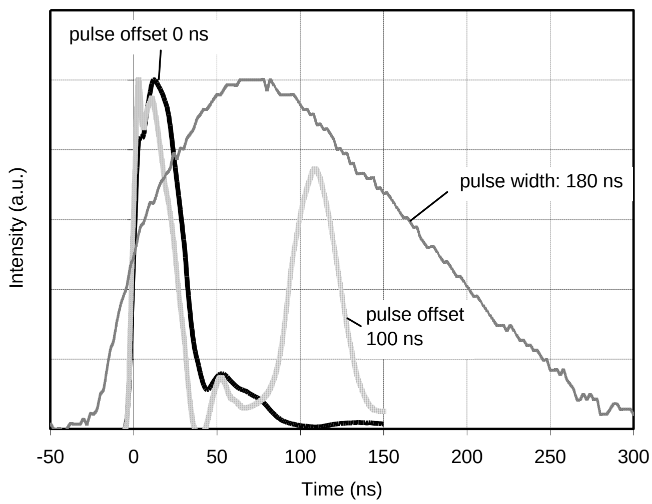

Figure 1.1. Pulse shapes from the double laser system at 0 and 100 ns pulse offsets, and Excico’s 180 ns pulse.

Table 1.1. Thermal and optical properties of silicon used in the simulations.

	Solid	Liquid
ρ [g/cm^3]	2.33	2.33
c [J/gK]	$0.81 + 1.3 \times 10^{-4}T - 1.26 \times 10^{4}T^{-2}$	1
k [W/cmK]	$0.235 + 4.45\exp(-T/247)$	$0.502 + 2.99 \times 10^{-4}(T-T_m)$
α [cm^{-1}]	10^6	10^6
R [-]	0.7	0.65
L_H [J/g]	1780	
T_m [K]	1687	

Temporal thermal profiles were calculated with a 1-D model considering transient heat conduction. The thermal properties of silicon were temperature dependent, the reflectivity was phase dependent, and the melting was incorporated into the model by the enthalpy method [1]. Transient heat conduction was considered with the governing equation:

$$\rho c^*(T)\frac{\partial T}{\partial t} = \frac{\partial}{\partial x}\left(k(T)\frac{\partial T}{\partial x}\right) + Q(x,t)$$

where ρ is the density of silicon, k is the thermal conductivity, T is the absolute temperature, t is time and x is the depth from the surface. The modified specific heat capacity, c^* is defined as:

$$c^*(T) = c(T) + L_H\delta(T - T_m)$$

where c is the specific heat capacity of silicon, L_H is the latent heat, and δ is the Dirac delta function, and T_m is the melt temperature of silicon.

The laser energy absorbed by the silicon, Q, is defined as:

$$Q(x,t) = (1 - R)I(t)\alpha\exp(-\alpha x)$$

where α is the absorption coefficient, R is the reflectivity of silicon, and I is the pulse intensity. The boundary conditions are isolation at the surface and constant temperature at the bottom of the substrate:

$$\left.\frac{\partial y}{\partial x}\right|_{x=0} = 0;\ T_{xmax} = T_0$$

The material properties are summarized in Table 1.1.

1.2 Results

Measured sheet resistances of the laser annealed As^+ at 15 keV, 5 x 10^{14} cm^{-2} implanted layer are shown in Figure 1.2 for the different laser anneals as a function of the total laser energy density. In the double laser system, each laser irradiates at the half of the total energy density. The sheet resistance is inversely proportional to electron charge, the active concentration, and the mobility. Active concentration is strongly dependent on the melt depth, therefore the sheet resistance decreases with the increasing laser energy density as the melt depth increases. To reach a sheet resistance of 300 ohm/sq, a total fluence of 600, 800, 1200 and 1850 mJ/cm^2 is needed for the different laser anneals a)-d), respectively. By using the double laser system, increasing pulse offsets will shift the sheet resistance curves towards higher energies, while the chuck or substrate heating will shift the curve towards lower energies with respect to the anneal with no offset at room temperature. As pulse offsets above 100 ns are less effective [Gonda et al., 2007], the fluence range for this particular implant can be tailored at 600-1200 mJ/cm^2. Further increasing the fluence for the same sheet resistance is only possible by increasing the laser pulse width. The results for an anneal with a 180 ns pulse is shown in Figure 1.2 with a dashed line. As the pulse width increases, the maximal intensity decreases and the thermal gradients decreased too. The reduced solid/liquid interface velocity may influence segregation processes [Wood et al., 1984]. These are beneficial for defect anneal and to avoid ablation [Venturini et al., 2003].

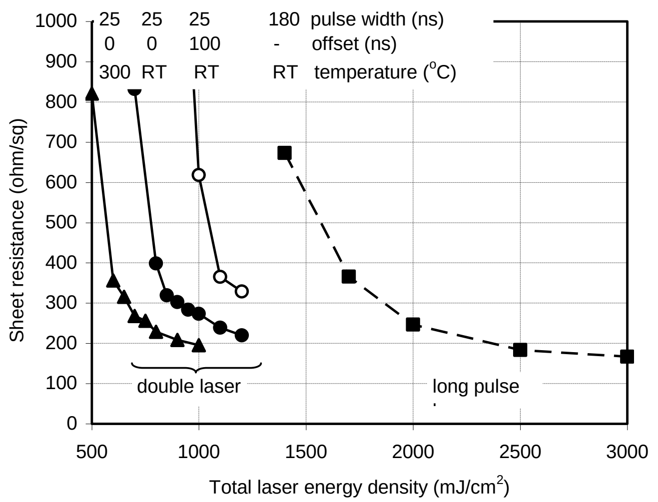

Figure 1.2. Measured sheet resistance of the As^+ at 15 keV, 5 x 10^{14} cm^{-2} implanted layer as a function of the laser energy density, laser annealed with a substrate at room temperature or 300°C, pulse width of 25 or 180 ns, single or double pulsed.

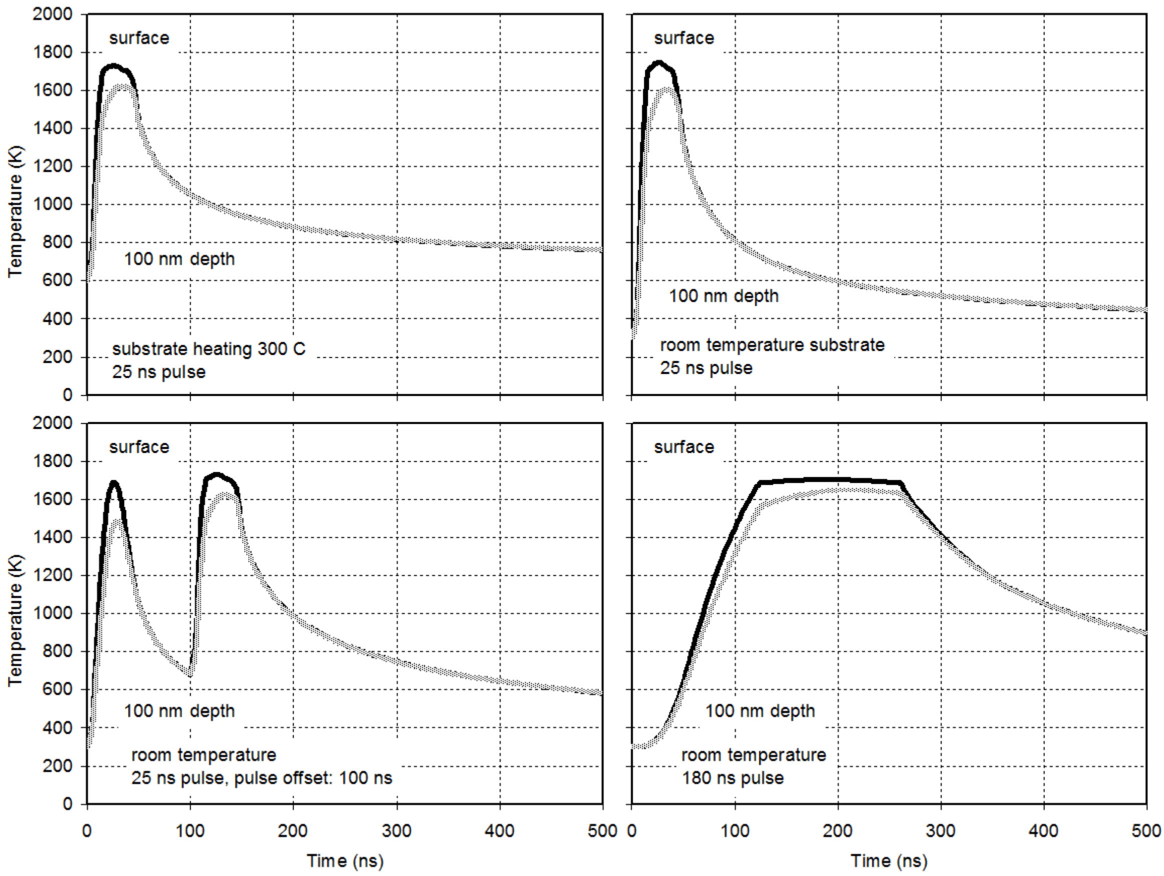

Figure 1.3. Calculated temporal thermal profiles at the silicon surface and at 100 nm depth for the different laser anneals.

Temporal thermal profiles were simulated for these anneals at a total fluence of 600, 800, 1200 and 1850 mJ/cm^2, respectively. The surface temperature and the temperature at 100 nm depth are shown in Figure 1.3. The maximum melt depth was 50 nm in each case, and the depth of 100 nm as a critical depth for the devices was chosen. In general, the thermal cycles that are induced by the laser pulse are much longer than the laser pulse itself, the temperature decay elongates the thermal cycle. In zero offset and the single shot anneals, the melt and regrowth, i.e. the complete activation occurs by a single pulse. In the double pulsed anneals with pulse pairs, melting might not reached at the first pulse, but as the second pulse arrives when the cooling is not completed, it has a temperature advantage, similarly as the case of the heated substrate. It is also seen that the time in the melt is slightly different for the different anneals. Moreover the temperature difference between the surface and in the depth is different during the melting, while this difference is vanished during cooling. As the melt depth reaches 50 nm, the maximum temperature can just reach the melt temperature of crystalline silicon, but not exceed it. For the ultra shallow anneals and tight thermal limitations, this difference should be large, while for defect anneal, and deep recrystallization this difference should be low. The extents of these anneals are the short and long pulse anneals, the long pulse anneal results about 50°C higher temperature at 100 nm depth than the short pulse anneal.

1.3 Conclusions

Various ultra short surface annealing thermal cycles were realized by double pulsed excimer laser annealing and long pulse excimer laser annealing. Full-melt energies can range from 600 to 1850 mJ/cm^2 were determined for on arsenic implanted silicon at 15 keV, 5 x 10^{14} cm^{-2} to demonstrate dopant activation with different energy depend on the substrate heating, the pulse width and shape. These parameters will also determine the temporal and spatial thermal gradients, which were determined by simulations. Conclusions are: (1) To fully activate the implanted As^+, a 25 ns pulsed laser anneal at room temperature requires 800 mJ/cm^2 fluence, and provides the smallest heat affected zone. (2) In double pulsed laser annealing, the heat pulse generated by the first laser pulse is longer than the delay between the laser pulses, therefore at short offsets the heat pulses are superposed. This way, thermal budget can be increased by 20-50% with the pulse offsets maintaining the melt depth. By using equal pulses at an offset of 100 ns, the first pulse heats, and the second pulse completes the activation, and the full activation can be reached at 600 mJ/cm^2/pulse. The thermal cycle of the second pulse resembles the cycle when the substrate was heated to 300°C. (3) Largest thermal budget can be realized with long pulse, which results in low thermal gradients, therefore large heat affected zone.

1.4 Proposition

Excimer laser annealing provides an ultimate rapid thermal annealing method for implanted dopants in semiconductors. While the lowest thermal budget is achieved by a short single laser pulse anneal, a double laser pulse process integration in silicon with pulse offsets allows control in overlapping heat pulses with decreased peak intensity and increased total energy [1][2][3][4].

2 Hot ductility variations within the continuously cast strand [5]

Along the metallurgical length in continuous casting, the temperature within the steel strand ranges from above melt temperature (>1500°C) down to about 900°C during the cooling. In this range, particularly in the mushy zone, mechanical properties drastically drop at above critical temperatures as the zero deformation temperature (ZDT) and the zero strength temperature (ZST) due to the presence of the liquid phase, therefore crack susceptibility increases. These critical temperatures depend on (local) chemical and microstructural properties.

We investigated the change in ZDT and ZST for ST52-3 steel grade by taking samples from the as-cast strand from positions of the columnar grains zone and from the segregated zone located at the centerline of the strand, to investigate the effect of the variations in chemical compositions. Samples were also taken from a hot rolled sheet with finer microstructure for a reference. We performed high temperature tensile testing to determine the mechanical properties, and analyzed the thermal and microstructural properties of the samples. We found more than 100°C drop in ZDT due to segregations in the centerline compared to the columnar zone within the strand.

2.1 Experimental procedures

The material used in the tests was ST52-3 steel in as-cast and hot rolled state. The chemical composition measured for the as-cast specimen taken from the homogeneous zone is shown in Table 2.1. We performed high temperature tensile testing to determine the critical temperatures for the loss of hot strength (ZST) and ductility (ZDT), we analyzed the specimen cross sections, and furthermore we measured and simulated thermal properties for the steel grade.

Samples were taken from the as-cast strand and from a hot rolled sheet. From the cast strand, a slice was cut perpendicular to the casting direction. Samples were taken from the columnar grain zone as well as from the segregated zone of the slice (Figure 2.1, left). From the hot rolled sheet, the samples were taken perpendicular to the rolling direction, from the center of the sheet. Cylindrical specimens were fabricated with a diameter of 10 mm and a total length of 117 mm (Figure 2.1, right). High temperature tension tests were performed in vacuum with the Gleeble 3800 system by using a low force jaw set. In order to maintain a flat temperature profile along the specimen axis, and also radially, a quartz tube was placed to the center of the specimen with a gap for the R-type thermocouple wires which were welded to the surface. Applied thermal and mechanical loads are shown in Figure 2.2. First the specimen was heated with a high rate to 1300°C, then held for 1 min, and subsequently further heated with a low rate to T_{tens} temperature, which was in the range of 1300-1440°C. After 1 min hold time, the tensile test started with a constant stroke speed of 0.1 mm/s. During the testing force, elongation, and the nominal (T_{tens}) and actual temperatures were recorded. This latter temperature, T_{tc} is always the one measured at the surface by the thermocouples.

After mechanical testing, selected specimens were prepared for metallurgical analyses with optical microscopy. Axial sections were cut of these specimens, the surface was polished, and etched with Nital for microstructure analysis.

For comparison, thermal properties were measured for the as-cast state (columnar zone) by Differential Thermal Analysis (DTA) on a Setaram Setsys 1750 analyzer. The heating and cooling rate was 10 K/s, there was a 5 min hold time at 1550°C, the testing was executed in Ar ambient with a sample weight of 553.4 mg. Thermal and structural properties were simulated by the IDS software for the chemical composition in Table 2.1.

Table 2.1. Measured chemical composition for as-cast ST52-3 in wt%.

C	Cr	Ni	Mn	Mo	Si	Nb	Ti	Cu	V	Al	P	S
0.166	0.085	0.051	1.45	0.004	0.308	0.004	0.003	0.086	0.008	0.04	0.02	0.012

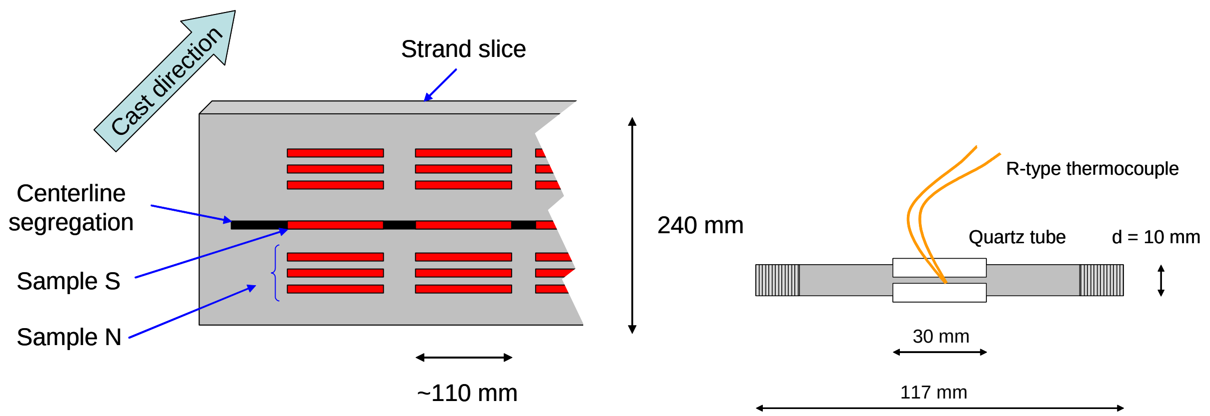

Figure 2.1. Locations of samples taken from the slice of the continuous cast strand (left). Tensile test specimen (right).

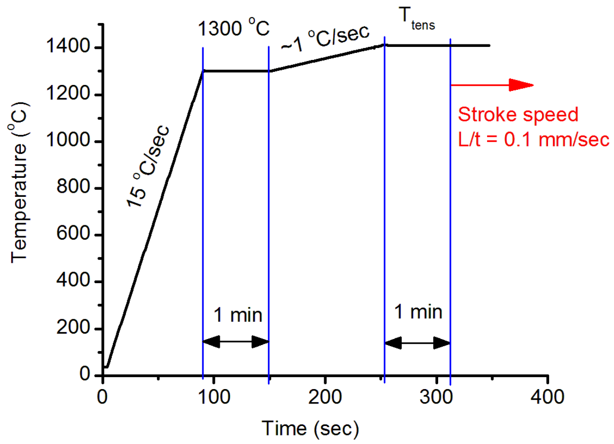

Figure 2.2. Nominal temperature versus time and the mechanical loading for the high temperature tensile test.

2.2 Results

High temperature tensile testing results are shown in Figure 2.3 for specimens taken from the segregated zone (a), the columnar grain zone (b) from the cast strand, and from a hot rolled sheet (c). The strain rate in these tests was about 10^{-2} s^{-1}. The strength and ductility might have a slight dependence on the rate [Seol et al, 2000]. At these surface temperatures, the elastic content of the deformation is very low, and the total deformation is considered as plastic deformation.

At relatively low nominal temperatures, eg. at 1380°C in Figure 2.3(b), uniform plastic deformation is apparent up to the ultimate strength, where necking of the specimen appears. Here ductility is very high, fracture occurs above 4 mm elongation (>20% strain), though strength decreases with increasing temperature. Approaching ZDT, ductility decreases and disappears within a 20-50°C interval. The loss of ductility is apparent in Figure 2.3(c) for 1405°C, where the force-elongations curve drops suddenly after the reaching the maximum force, as the specimen breaks without reduction in cross sectional area (RA), as seen on the photograph of the specimen in the inset. Further increasing the temperature, the strength drops quickly, ultimately to zero at ZST.

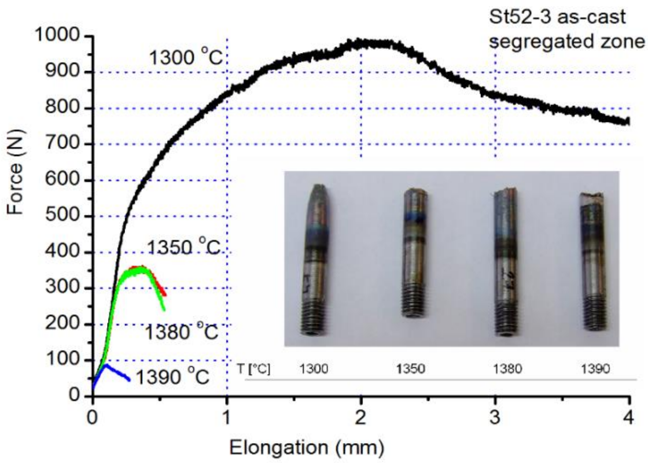

(a)

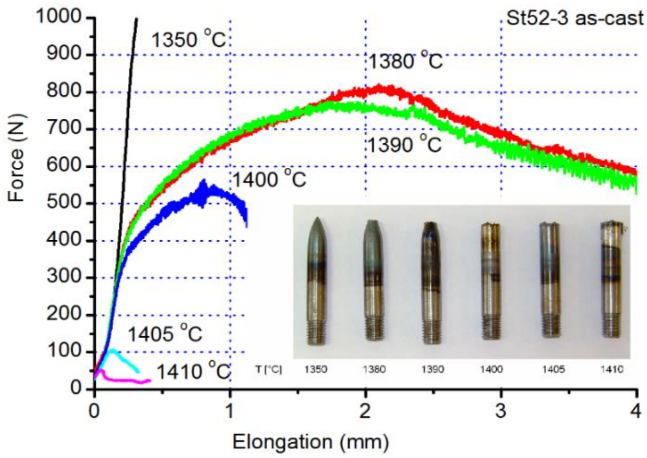

(b)

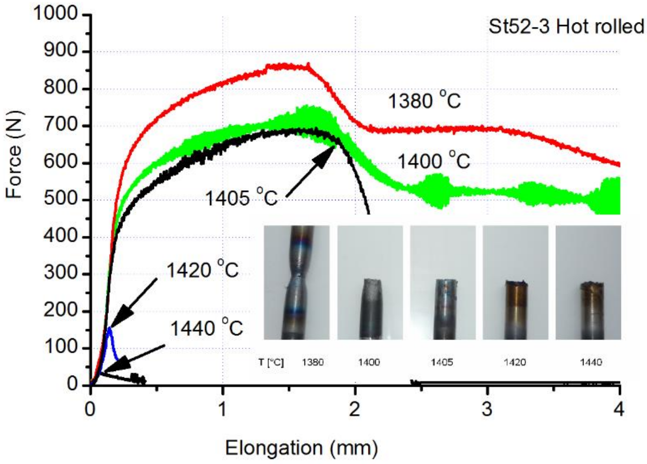

(c)

Figure 2.3. Force-elongation curves recorded at high surface temperatures for specimens taken from the segregated zone (a), the columnar grain zone (b) from the cast strand, and from a hot rolled sheet (c).

(a) 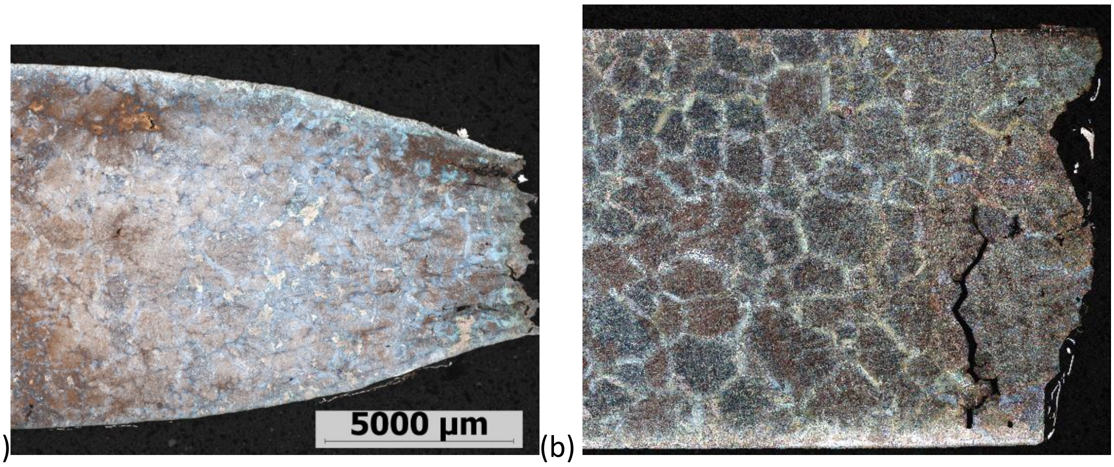

(b)

Figure 2.4. Micrographs (Nital etched) shown for as-cast specimens taken from segregated zone at T_{tens} = 1300°C (a), and from columnar zone at T_{tens} = 1405°C (b).

Micrographs are shown in Figure 2.4 for the as-cast specimen taken from segregated zone (a), and from columnar zone (b). For the latter, the test was conducted at 1405°C, this lies in between ZDT and ZST. Here ductility is lost, therefore the lack of RA, the fractured surface is abrupt and sharp. The corresponding microstructure is shown for the Nital etched surface: the austenite grain boundaries are apparent; also that fracture occurred along the grain boundaries. These are the locations, where the liquid phase appears first during the heating. A crack along the grain boundaries inside the specimen is also captured. Even the sample was taken from the columnar zone, the as-cast specimen contains some voids which are visible. Inspecting the micrograph for the sample taken from the segregated zone in Figure 2.4(a), tensile tested at 1300°C, Oberhoffer's reagent etched surface (now shown) reveals P segregations, as Cu precipitates from the reagent over P rich areas, the composition of the sample is very non-uniform. On the Nital etched surface, voids and inclusions are visible. Especially, S and P segregations along the grain boundaries reduce the critical temperatures significantly [Suzuki et al, 1984].

DTA test results are shown in Figure 2.5. During the heating, the gamma-delta transformation or the onset of the peritectic reaction occured at 1487°C. The peritectic reaction ended at 1511°C, and the liquidus was found to be at 1530°C. During the cooling the delta phase appears at 1496°C and there is a peak for the peritectic reaction at 1475°C.

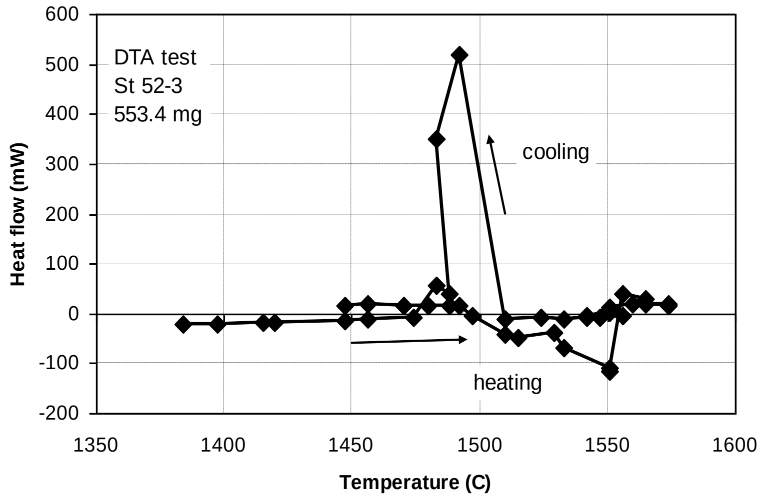

Figure 2.5. Measured thermal properties of as-cast ST52-3 (columnar zone) by using DTA testing.

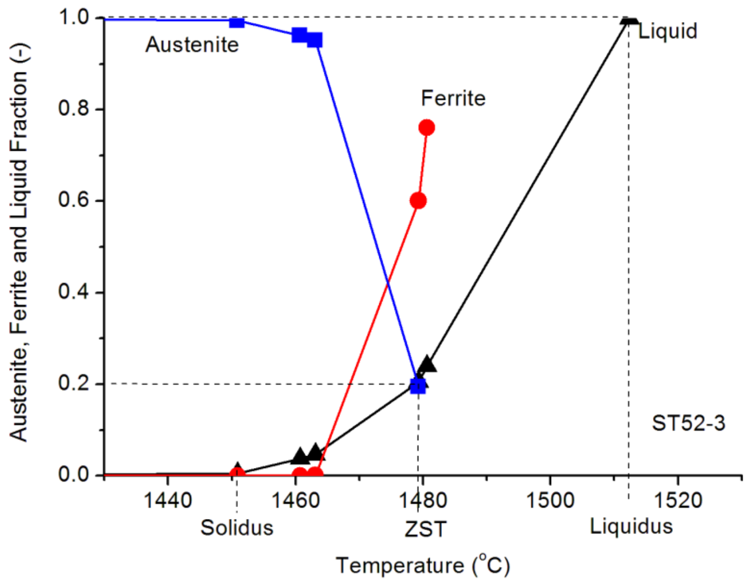

Figure 2.6. Simulated phases of austenite, delta-ferrite and liquid in IDS for ST52-3, with chemical composition given in Table 2.1.

Simulation results from the IDS software are shown in Figure 2.6. The liquidus and the solidus are at about 1510°C and 1450°C, respectively, ZST is determined for a liquid fraction of 0.2 to be 1480°C, and the gamma-delta transformation occurs in the mushy zone.

The DTA measured and simulated temperatures agree reasonably well. Nevertheless, the measured ZST and ZDT temperatures from the hot tensile tests are about 50°C lower than expected from simulations or from DTA measurement. Such difference was reported by [Seol et al., 2000], who measured central and surface temperatures by thermocouples on a specially prepared specimen. Though temperatures in the specimen are expected to vary radially, no clear evidence was found in the microstructure, while temperature clearly drops out of the hot zone laterally as austenite grain size drops accordingly.

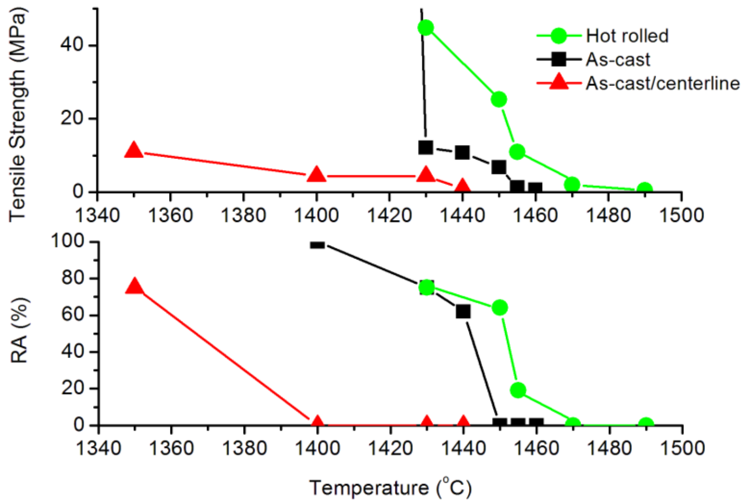

	ZDT (°C)	ZST (°C)
Hot rolled	1470	1490
As-cast	1450	1460
As-cast/cl	<1400	1440

Figure 2.7. Strength and ductility versus the corrected temperature of ST52-3 in as-cast and hot rolled state.

High temperature strength and ductility results of ST52-3 in as-cast and hot rolled state are summarized in Figure 2.7, the temperatures were corrected according to the simulation results. ZST and ZDT values are the highest for the hot rolled material, somewhat lower for the as-cast sample taken from columnar grain zone, and much lower for the as-cast sample taken from the centerline segregated zone of the strand. These variations can be explained by the local differences in the chemical composition, as the centerline zone is rich in P and possibly S segregations, and discontinuities, therefore the low critical temperatures, eg. ZDT < 1400°C. Hot rolled specimen has finer microstructure, therefore the higher critical temperatures. For continuous casting of ST52-3, the examined grade has safely high critical temperatures if S and P cannot segregate close to the surface of the strand.

2.3 Conclusions

By investigations of thermal and mechanical properties in the cross section of an ST52-3 continuously cast strand, the following conclusions can be drawn: (1) The ZST and ZDT temperatures measured at the surface of the specimen in the tensile tests are about 50°C lower than expected from simulations or from DTA measurement, therefore a temperature correction in necessary. (2) Temperatures in specimen are expected to vary radially, but no clear evidence was found in the microstructure, while temperature clearly drops out of the hot zone laterally as austenite grain size drops accordingly. (3) ZST and ZDT values are the highest for the hot rolled material, somewhat lower for the as-cast sample taken from columnar grain zone, and much lower for the as-cast sample taken from the centerline segregated zone of the strand. (4) Fractured surface looks brittle above ZDT, cracks propagate along austenite grain boundaries. For continuous casting of ST52-3, the examined grade has safely high critical temperatures if S and P cannot segregate close to the surface of the strand.

2.4 Proposition

During the solidification in continuous casting, the moving solid-liquid interface pushes contaminants towards the centerline of the strand. In the centerline segregated zone, critical temperatures as zero strength temperature and zero deformation temperature drop significantly [5].

3 Strength of electromagnetic formed joints [6]

Electromagnetic forming is one of the high strain rate forming processes where deformations are completed within a fraction of a second. It is categorized within the group of electro-dynamic forming processes. Here controlled discharging of capacitor banks provide power to an electromagnet, in which a sufficiently high electromagnetic force is generated to be applied for metal forming. This technique has been developed to process sheet and tubular metal workpieces of good electrical conductivity and low yield strength.

In the case of tubes and hollow profiles, the compression or expansion methods of electromagnetic forming might be applied. The forming can also be carried out as a so-called free forming, but for the most workpieces a die is needed. This can be a mandrel core for compression tube forming; or a shaped ring for expansion tube forming. A frequent industrial application of electromagnetic forming is joining by electromagnetic compression of tubular parts. The goodness of the joints is determined by the strength of the joint, and it is considered excellent if it reaches the strength of the weaker material. Strength of these joints are generally tested for tensile and torsion loadings. In order to increase strength, one or more horizontal and/or radial grooves can be fabricated onto the male joining pair to utilize form fitting besides interference fit, and it is important to find the electromagnetic forming energy that provides sufficient deformations of the contacting pairs [Weddeling et al., 2011].

Modeling of the processing is twofold: coupled electromagnetic and mechanical modeling of the electromagnetic forming requires large computational resources, where electromagnetic part has much higher computation costs than the mechanical calculations. Subsequently, mechanical modeling of joint strength reveals (in)sufficient deformations originated from the joining stage.

In this work, joining of tubular parts are demonstrated by using radial and axial grooves to employ interlocking by form fitting. Furthermore, a computational cost effective modeling is developed with uncoupled mechanical modeling of the electromagnetic forming by calculating the applied forming pressure with an equivalent circuit model; and subsequently modeling the tensile testing to evaluate the goodness of the joint.

3.1 Experimental and modeling procedures

A schematic setup of a compressive electromagnetic tool is shown in Figure 3.1. In the experiments, S-Metalltech's EMA-EHA-EM 24/30 forming tool equipped with a field shaper of 60 mm working die-hole length was employed. The charging voltage was set to 5.8 kV, resulting in a charging energy of 12.0 kJ for aluminum processing. The duration of the deformation is very short (0.1-1 ms), while the deformation rate of the workpiece material can reach about 50-300 m/s. The high deformation rate leads to a very high strain rate, in the range of 10^2-10^4 s^{-1}.

For the contact pairs, 3103 H111 Al alloy tubes and 6060 T6 Al alloy rods were selected. Up to three radial and axial grooves were machined onto the contacting end of the rods to create high strength joints for both for axial tension and radial torsion loadings [Rácz et al., 2014]. The schematics of a joint before processing is shown in Figure 3.2.

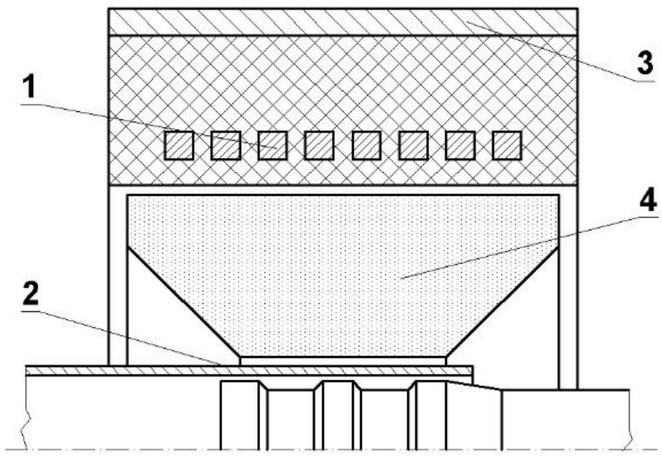

Figure 3.1. Schematics of the compressive electromagnetic forming tool with field shaper (1: coil, 2: workpiece, 3: metal case, 4: field shaper).

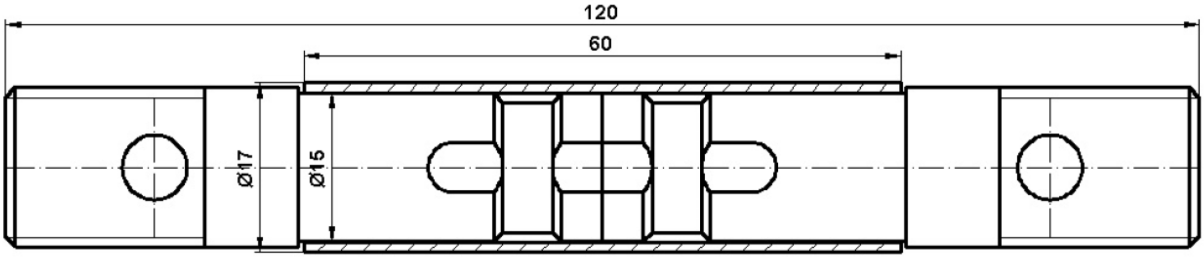

Figure 3.2. Joint schematics with one radial groove.

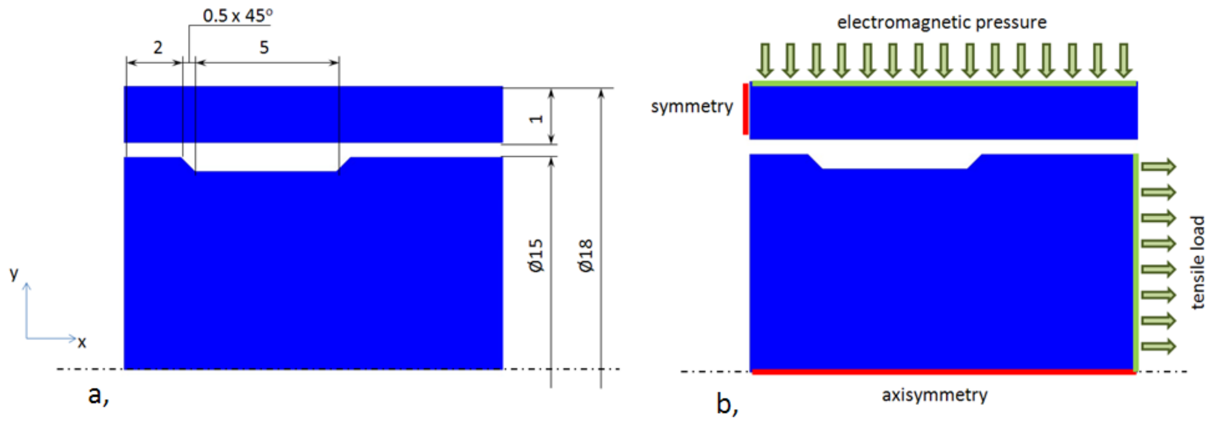

Figure 3.3. Modeled geometry of the joint pairs showing (a) dimensions, and (b) loading and constraints of the modeled tubular joint.

In the numerical simulations, forming of a joint with one radial groove and the subsequent tensile testing was implemented. A schematic of the geometry is shown in Figure 3.3. Axisymmetry was employed and half of the assembly was modeled.

Both materials in the simulations were modeled as linear elastic—linear hardening plastic type. The elastic properties were the elastic modulus of 70 GPa, and Poisson's ratio of 0.33 for both parts. The plastic properties for Al 3103 were: yield strength of 35 MPa, hardening coefficient of 325 MPa, tensile strength of 100 MPa at 0.2 strain; and for Al 6060: yield strength of 150 MPa, hardening coefficient of 500 MPa, and tensile strength of 200 MPa at 0.1 strain. The Coulomb friction coefficient was 0.3 between the contacting pairs.

A simplified modeling of the electromagnetic forming was implemented with pure mechanical modeling and quasi-static loading, considering computational cost effective simulations [Mamalis et al., 2005]. The electromagnetic pressure was applied as a mechanical pressure boundary condition.

In electromagnetic forming, the electromagnetic pressure is a decaying sinusoidal time function. A relationship can be derived by modeling the actual electromagnetic forming equipment using an equivalent electromagnetic circuit formulation [Göbl, 1978] considering a constant airgap. For compression forming, the electromagnetic pressure, p_m, is given as:

$$p_m = A \cdot (\exp(-B \cdot t))^2 \cdot \sin^2(C \cdot t) \qquad [\mathrm{N/mm^2}] \qquad (3.1)$$

where t is time, and A, B, C are constants. These constants were calculated for the charging voltage, their values corresponding for 1 to 9 kV can be found in Table 3.1.

Table 3.1. Values of the constants for Eq. 3.1.

U [kV]	1	2	3	4	5	6	7	8	9
A	2.242	8.967	20.177	35.87	56.04	80.71	109.85	143.48	181.59

B=6882.73, and C=45659.49

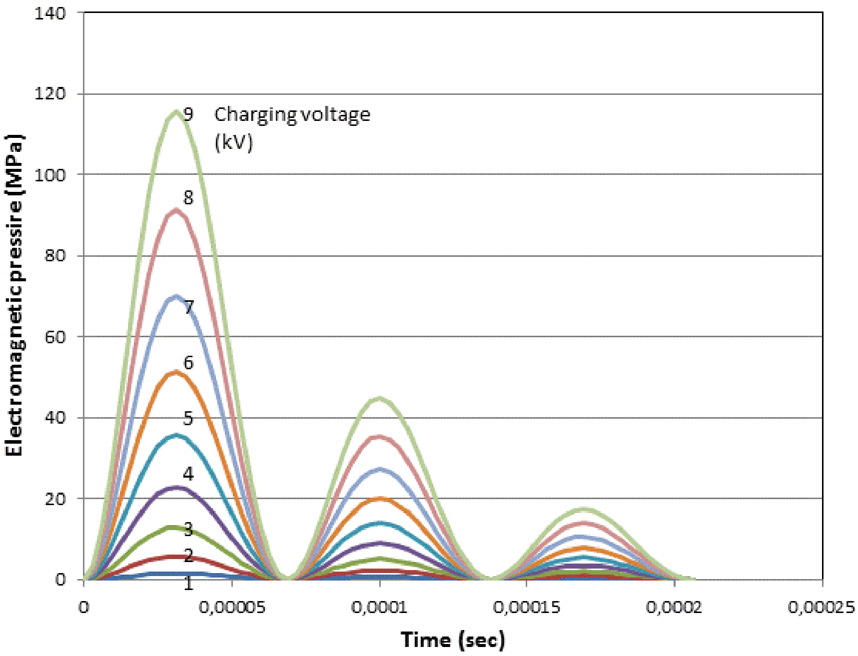

(a)

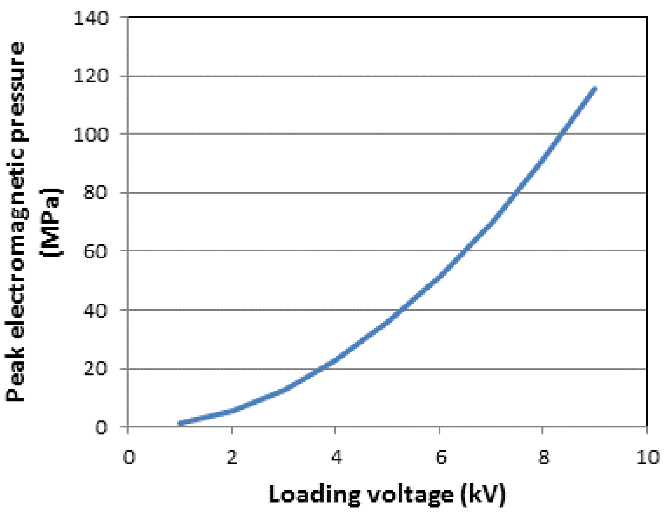

(b)

Figure 3.4. Electromagnetic pressure in time as a function of the charging voltage (a), and the peak pressure at the first pulse as a function of the charging voltage (b).

The time function of the electromagnetic pressure for different charging voltages is shown in Figure 3.4(a) for the first 3 pulses. The peak pressure achieved at the first pulse at about 25 µs is shown in Figure 3.4(b) as a function of the charging voltage.

In the model, only the first loop was taken into an account, because the subsequent peaks are much weaker, and the air gap is increasing with the deformation. The shape of the peak was approximated as being triangular with a peak intensity of 40 MPa. Subsequently, an axial tensile load was applied onto the rod, simulating the tensile testing of the joint.

3.2 Results

The internal structure of the fabricated joints were investigated by X-ray tomography as shown in Figure 3.5. A joint section is shown with one radial groove and three axial grooves were machined. It can be seen that the wall of the tube has not been deformed in the extent required to entirely fill the grooves. Despite this fact, the measured tensile strength of the joints was acceptable as testing showed [Rácz et al., 2014]. In the tensile tested joints, there was a significant plastic deformation before fracture. Joints made with one radial groove could not withstand the tensile load up to the fracture of the tube; rods were pulled out from tubes. Joints with two radial and three axial grooves fractured at loads of 5.5-5.8 kN.

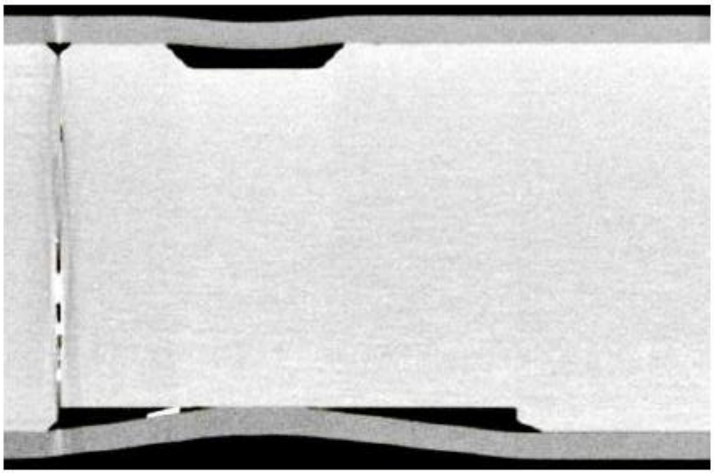

Figure 3.5. X-rays tomography picture of a joint with one radial groove [Rácz et al., 2014].

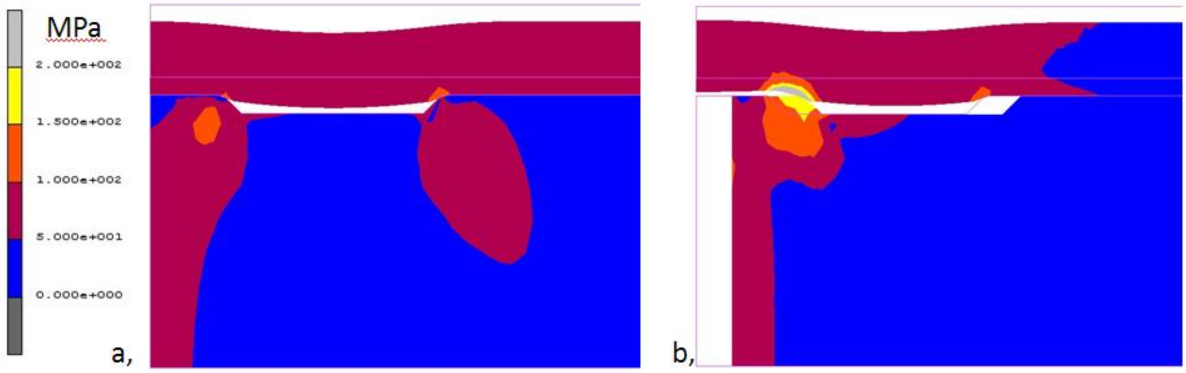

Figure 3.6. Equivalent stresses (a) at the peak of the electromagnetic pressure pulse, and (b) during tensile loading of the rod.

Simulation results for the equivalent stresses are shown in Figure 3.5. At 40 MPa loading, the tube was deformed into the groove, but not filling in entirely. Its plastic deformation was sufficiently large to employ both form fit and interference fits. In tensile testing of the fit, the rod would slide out of the tube, this case the strength of the tube was below the strength of a weaker part, which was the tube. This was also proved experimentally [Rácz et al., 2014]. For employing 3 radial grooves, the strength of the joint was shown to reach the strength of the tube.

3.3 Conclusions

Based on the experiments on electromagnetically formed tubular joints and on the simulations of the forming and testing processes, the following conclusions can be drawn for Al/Al joints: (1) the two and three radial grooves significantly improved the tensile strength of the joint even at low compression deformation and weak groove filling. (2) The decoupled modelling approach resulted similar deformations as in the experiments, with low computational costs.

3.4 Proposition

High strength tubular joints can be produced by electromagnetic forming. Combining form fit with interference fit in the design of the joints, joint strength at the ultimate strength of the tube material is reached at low forming pressure with small deformations [6].

4 Stored energies in highly strengthened metals [7]

Large amount of strengthening can be achieved by equal channel angular pressing (ECAP), through the applied severe plastic deformation during the processing. For pure metals, this high strength is accompanied with low thermal stability due to the uninhibited driving force for recrystallization by the large stored energy.

In ECAP, the applied deformation is determined by the geometry of the extrusion die and the number of passes [8], nevertheless the microstructural changes and the stored energies are also dependent on the processing routes [Sarkar et al., 2012] as well as on the processing temperature besides the initial state of the material. By ECAP, high material performance is achieved [9], which can be optimized by pre- or post-processing heat treatments. Near saturation strain hardening initiated grain refinement contributes to the overall strengthening of the material in ECAP processing. Due to the large applied deformation, the stored energy is high, therefore the driving force for recrystallization is high, resulting in low thermal stability [Molodova et al., 2007]. For this reason, thermal stability of pure metals processed by ECAP are extensively studied [Higuera et al., 2011] [Balogh et al., 2006] [Hegedűs et al., 2013]. In the present work, the chosen technological route was elevated temperature single pass ECAP processing of copper and its effect on the thermal behavior during the restoration processes of the deformed samples was studied.

4.1 Experimental procedures

Commercially available pure Cu was used as a starting material. The initial shape was a drawn rod, from which cylindrical specimens of 10 mm diameter and 60 mm length were machined. Prior to ECAP, the specimens were annealed at 450°C for 1h. ECAP processing was performed by single pass at temperatures of room temperature, 50°C, 100°C, 150°C, and 200°C, two pieces for each temperatures. The ECAP die was constructed with a channel angle of 110° with sharp corner, hence the equivalent strain was 0.8 in one pass. Molycote grease was used for lubrication, and the velocity of the cross head was set to 8 mm/min in a screw driven machine. The experimental setup is shown in Figure 4.1. From the processed specimens, coin shaped samples of 6 mm in diameter and 1 mm height were machined for differential scanning calorimetry (DSC) measurements. Different continuous heating rates of 5, 10, 20, and 50°C/min were set in a Perkin Elmer DSC 8000 calorimeter to heat the samples above the recrystallization temperatures up to 400°C. Specific heat flux was measured, then the recrystallization peak temperature, the stored energy, and the activation energy were calculated for the samples. Hardness was measured on a Zwick tester with Vickers head and 2.2 kgf load, both after ECAP processing, as well as after the annealing in DSC.

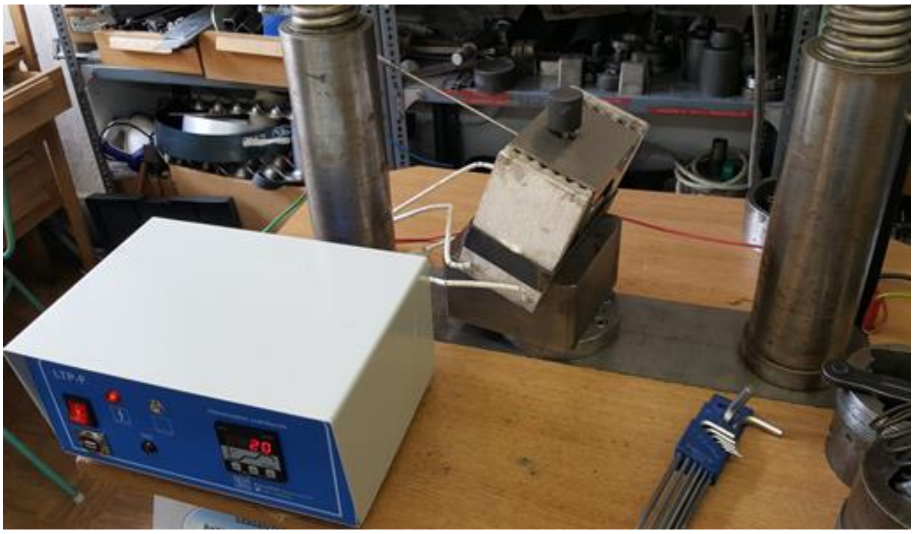

Figure 4.1. Experimental setup for the ECAP processing with a heated die.

4.2 Results

Specific heat flux data were collected by the DSC measurements, and baseline compensation was applied. A processed DSC measurement result is shown in Figure 4.2 for recrystallization peak temperatures at a heating rate of 10°C/min as a function of the ECAP processing temperature. The increasing processing temperature pushes the recrystallization peak from about 233°C (room temperature processing) to higher at about 250°C (200°C processing temperature) for the same heating rate.

The recrystallization peak areas were calculated for each samples' DSC data. These areas correspond to the stored energy in the material. This stored energy is directly related to the energies stored in the grain boundaries and dislocations and these are released during the annealing process [Hegedűs et al., 2013]. Stored energy calculated from DSC data at a heating rate of 10°C/min as a function of the ECAP processing temperature is shown in Figure 4.3. The stored energy decreases from about 560 mJ/g at room temperature processing, with the increasing processing temperature until 150°C, then remains about a constant value of 400 mJ/g to the highest processing temperature of 200°C.

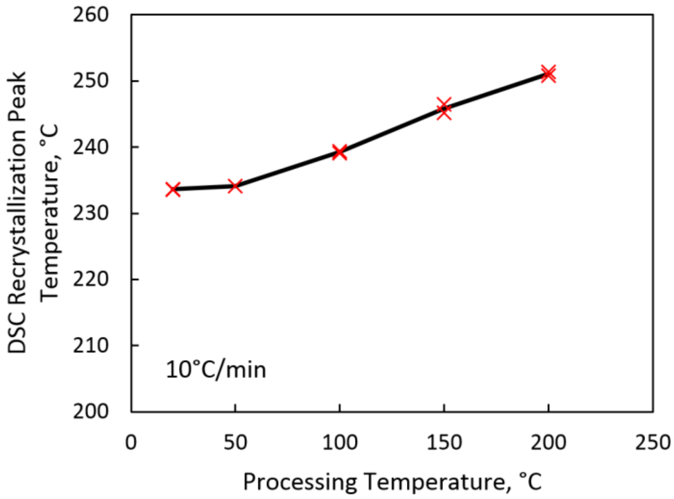

Figure 4.2. Recrystallization peak temperature measured by DSC at a heating rate of 10°C/min as a function of the ECAP processing temperature.

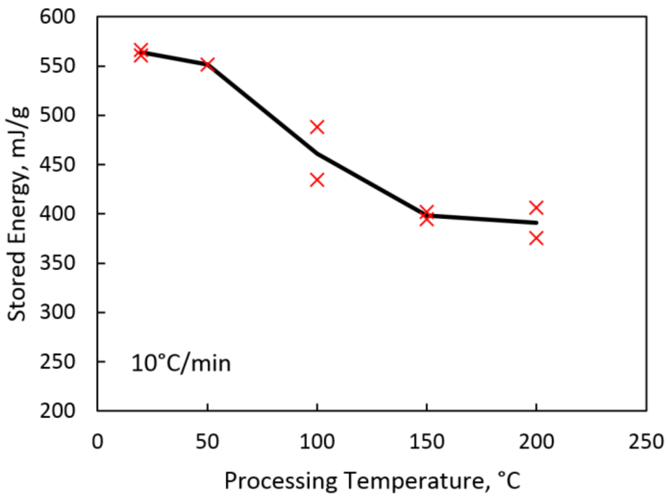

Figure 4.3. Stored energy calculated from DSC data at a heating rate of 10°C/min as a function of the ECAP processing temperature.

The energy stored in dislocations (E_d) can be calculated by the following equation [Hegedűs et al., 2013]:

$$E_d = A\frac{Gb^2\rho}{\rho_m}\ln\frac{1}{b\sqrt{\rho}}$$

where A is $(4\pi)^{-1}$ for pure screw and $(4\pi(1\text{-}0.3))^{-1}$ for pure edge dislocation, G is the shear modulus, b is the Burgers vector, ρ is the dislocation density, ρ_m is the mass density. In the first ECAP pass at room temperature for copper, the dislocation density is about 1×10^{15} m^{-2} [9] [Balogh et al., 2006], therefore the calculated value for E_d is about 300-400 mJ/g. Comparing to the DSC results, which are larger [Balogh et al., 2006], it suggests that other components may contribute to the released energy in the samples. The additional contribution from the energies stored in high angle grain boundaries and twin boundaries may be too small to count for the deviation [Hegedűs et al., 2013].

The effect of the heating rate on a sample processed at a given temperature results in increasing peak temperatures as well. From these results, the Arrhenius plot were constructed and activation energies of the recrystallization process were determined. The activation energies were calculated by the Kissinger method [Benchabane et al., 2008]:

$$\ln\left(\frac{T_p^2}{\beta}\right) = \frac{E_a}{R}\frac{1}{T_p} + c$$

where T_p is the peak temperature, β is the heating rate, E_a is the activation energy, R is the universal gas constant, and c is a constant.

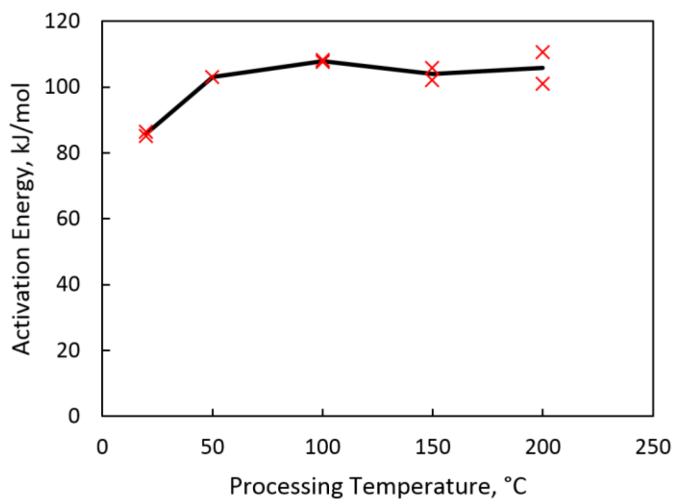

Figure 4.4. Activation energies calculated from DSC data as a function of the ECAP processing temperature.

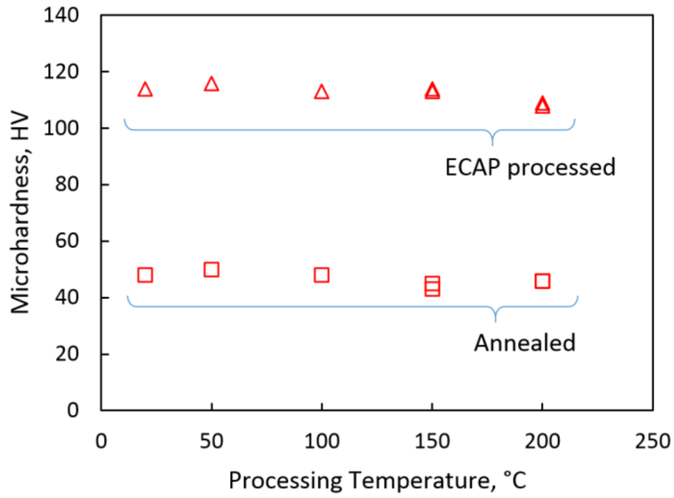

Figure 4.5. Measured microhardness of as-processed samples by a single pass ECAP, and after annealing in DSC as a function of the ECAP processing temperature.

Activation energies calculated from DSC data as a function of the ECAP processing temperature are shown in Figure 4.4. Activation energies increase from about 85 kJ/mol at room temperature processing up to about 110 kJ/mol until the processing temperature of 100°C, then remain constant.

Measured hardness values shown in Figure 4.5 for the as-processed samples were about constant of 115HV with the processing temperature, only a slightly decreased value of 109HV was measured for the 200°C processing temperature. The annealed samples have the same hardness at about 46HV, independently of the ECAP processing temperature in the tested range.

4.3 Conclusions

Upon the thermal analysis of the single pass ECAP processed copper at elevated temperatures, the following conclusions are drawn: (1) By increasing the ECAP processing temperature even up to 200°C, during the deformation, as shown by the increasing recrystallization peak temperatures and the decrease of the stored energy of the DSC measurements. (2) Activation energies calculated by the Kissinger method increase from 85 kJ/mol to 105 kJ/mol with the process temperature from room temperature to about 100°C, then remains at about the same level up to 200°C. (3) Based on the hardness measurements, as-processed sample hardness remains constant up to 150°C processing temperature, then a slight reduction is seen. The annealed samples possess the same hardness independently of the ECAP process temperature. (4) The thermal stability of the samples slightly increases with the increasing processing temperature, as activation energy increases, while high strength is maintained, as as-processed sample hardness remains nearly constant.

4.4 Proposition

Material performance is highly increased by single or multiple equal channel angular pressing at room temperature. At elevated temperature processing below the recrystallization temperature, the plastic work decreases due to the decreasing yield strength while the magnitude of deformation is unchanged, resulting in smaller stored energy without a significant hardness change [7][8][9].

5 Inherent strain modeling for metal additive manufacturing [10]

Common processes for additive manufacturing technology for metal components are laser heating/melting processes, such as selective laser melting (SLM), which can be executed on steels [Langi et al., 2021][Radhamani et al., 2021] as well as on advanced alloys [Bean et al., 2019]. In SLM, a metal powder layer is applied to the heated surface of the base plate of same material quality, and the corresponding layer of the model geometry is irradiated to melting by a laser. It continues layer-to-layer until the part is completely built. The unused metal powder is removed from the working area, then the base plate is unmounted, if necessary, heat treatments are performed, and the printed part is separated from the build plate. Finally, the supporting structure is removed from the workpiece.

During the process, different thermal loads are exposed to different parts of the workpiece: in some locations there is less constrain towards thermal expansion than in others, resulting in a distribution of inhomogeneous residual stresses over the piece, causing the printed geometry may deviate from the designed one. It is worth estimating the deformations before printing by simulation, which makes it possible to adjust the geometry for the workpiece and/or supports based on these estimated deformation results.

Simulations of additive manufacturing processes require high computational power, therefore simplifications and assumptions are established about modeling, to the extent that the accuracy of the estimate is still acceptable. Related to the geometry, meso/macro scale simulations are considered for the simulations of the printing process, and from a physical point of view, it is possible to use solely a mechanical model to estimate the deformations within a relatively short computational time. The key to the physical simplification is the application of inherent strains [Ueda et al., 1993], that is the source of the residual stresses, and it can be considered as a calibration parameter for a specific material quality, machine, and process parameter set [Setien et al., 2019][Lu et al., 2019]. Determination of inherent strains require complex procedures [Liang et al., 2019], or special specimens which are used with a simulation feedback loop for iterative refinement of results [Simufact, 2020].

In this computational study, the effect of the magnitude of inherent strain is examined for the simulated deformations of a printed specimen, where the material grade is either of MS1 or 316L steel powders. Even both material qualities are steels, and the same sets of inherent strain values with different magnitude and directional variations are chosen, allowing isotropic and orthotropic behavior too, the resulting deformation in the printed part may also be strongly influenced by the elastic/plastic mechanical properties of the different steel grades.

5.1 Modeling procedures

Inherent strain method was originated in determination of welding deformations with an efficient way [Ueda et al., 1993]. It is very time consuming to simulate large welded structures – as well as multi layered additive manufactured parts by coupled thermo-mechanical analysis. Inherent strains method is an approximate alternative for the simulation of welding and additive manufacturing simulations where residual deformations are in the main focus. Numerous studies were performed on welding [Deng et al., 2007][Hill et al., 1995][Kim et al., 2015][Ma et al., 2016]. Recently, it has been successfully applied on modeling additive manufacturing [Setien et al., 2019][Lu et al., 2019][Liang et al., 2019].

In additive manufacturing, when cooling after laser irradiation is reached, the resulting strain ε may have elastic ε_e, plastic ε_p, thermal ε_t, creep ε_{cr} and phase transformation induced strain ε_{ph} components as:

$$\varepsilon = \varepsilon_e + \varepsilon_p + \varepsilon_t + \varepsilon_{cr} + \varepsilon_{ph}$$

Inherent strain ε_i, is defined as the difference between the deformation strain and the elastic strain, therefore it can be written as:

$$\varepsilon_i = \varepsilon_p + \varepsilon_t + \varepsilon_{cr} + \varepsilon_{ph}$$

Inherent strains are typically applied as mechanical boundary conditions in the calculations for the layer, which is subjected to high temperature during the additive manufacturing simulation process to capture the structural response at the end of the deposition step. The structure can be treated as elastic-plastic with the inherent strains applied either over a number of increments or as a one-increment total value in the finite element analysis. The actual layer thickness in the simulations can be larger than the real layer thicknesses to reduce calculation costs, following a meso/macro scale approach to estimate deformations with reasonable accuracy.

The actual values of inherent strain components ε_{i-x}, ε_{i-y}, and ε_{i-z} in the simulations are taken as calibration parameters. For the calibration, dedicated comb test structures might be used in correspondence with the special calibration routine of the

Simufact Additive simulation software [Simufact, 2020] or other procedures described in [Setien et al., 2019][Liang et al., 2019][Hill et al., 1995].

In the present study, the finite element software of Simufact Additive 2020 [Simufact, 2020] was used for the simulations. The workpiece was a U-Charpy specimen with dimensions of 55 mm × 10 mm × 10 mm with a U-notch of 2 mm wide and 5 mm deep. Orientations of the workpieces were 0°, 45°, and 90° with respect to one axis of the build plate as shown in Figure 5.1. A measurement point is defined on each specimen at the corner shown in Figure 5.2, where x and y displacement data were collected at the end of the simulations.

Pure mechanical simulations were executed of the manufacturing process stages of build, release of the build plate and removal of the supports. Base plate deformations were considered in the simulations. Generic machine definitions with a build space of 250 mm × 250 mm × 250 mm were used, where the build plate occupied the planar dimensions with a thickness of 30 mm of identical material grade as the specimens. Specimen geometric parts are imported from 'stl' files, support structures of 2 mm height were generated and the assembly was positioned over the build plate.

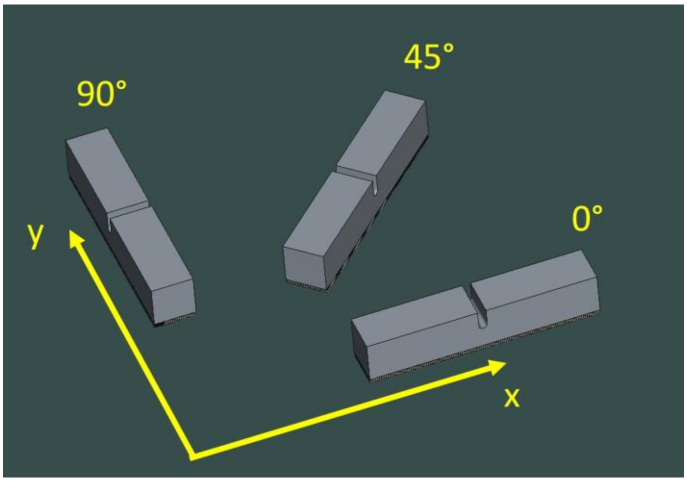

Figure 5.1. Orientations of the specimens on the build plate.

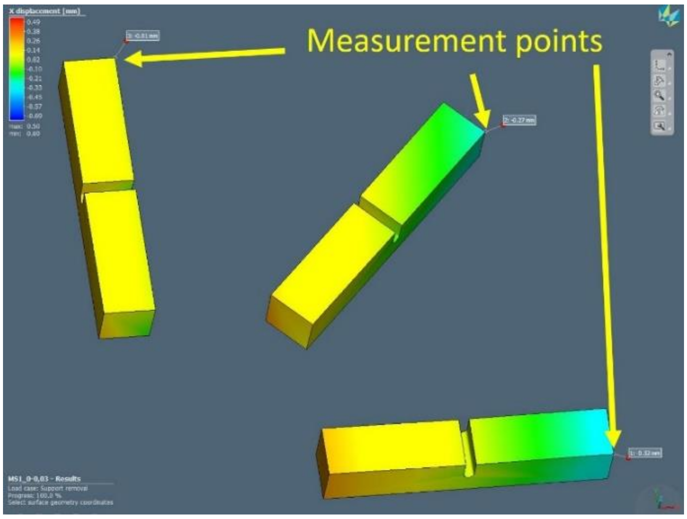

Figure 5.2. Measurement points for x and y displacements.

For the build parameters, a layer thickness of 0.03 mm was chosen. Uniform voxel size was set to 1 mm for the build space, and 4 mm for the base plate. All together 31292 voxels with 42277 nodes were generated in the simulation space.

Material properties were taken from the Simufact Material interface, where MS1 and 316L steel powder material property sets are available. MS1 is a maraging tool steel (material number: 1.2709, chemical notation: X3NiCoMoTi18-9-5); according to the EOS datasheets [EOS, 2017] its yields strength is $R_{p0.2}$ = 2010 MPa; ultimate tensile strength is R_m = 2080 MPa, and elongation at fracture is A = 4%. Material 316L is an austenitic stainless steel grade (material number: 1.4404, chemical notation: X2CrNiMo17-12-2); according to the EOS datasheets [EOS, 2017] its yields strength is $R_{p0.2}$ = 490-535 MPa; ultimate tensile strength is R_m = 590-650 MPa, and elongation at fracture is A = 35-45%. As both materials are steel grades, elastic properties are highly similar: Young's modulus was about 190 GPa; Poisson's ratio was 0.3 and density was about 8000 kg/m^3 for both materials. Flow curves for MS1 at room temperature in the simulations only scale to a plastic strain of ε_p = 0.007, while yield strength is in the range of about 1500-1900 MPa. Flow curves for 316L at room temperature in the simulations scale up to a plastic strain of ε_p = 0.2, while yield strength are in the range of about 600-700 MPa.

The inherent strain distribution was considered as uniform in the build space, with the planar ε_{i-x} and ε_{i-y} values varied in {0; -0.003; -0.016; -0.030} while off-plane value of ε_{i-z} was set to -0.030 in all simulations. This parameter variation resulted in 16 simulations for one material, all together 32 simulations.

5.2 Results

Stress-strain analysis reveals (details not shown here) that in the build parts the strains are the highest at the U-notch, and a slight plastic deformation occur in the parts at the bottom near the supports, while the upper region of the specimen is less loaded internally. In the MS1 specimens, the maximum of yield stress is about 1870 MPa, and in the 316L specimens, the maximum yield strength is about 680 MPa.

Results for the planar displacements at the measurement points are shown in Figure 5.3 and Figure 5.4 for MS1 and 316L specimens, respectively.

By comparing the planar displacements with respect to the orientations of the MS1 specimens, the following can be found: for 0° orientation, the specimen's long axis is parallel to the x axis; with increasing the x and y inherent strains magnitude, displacement in x direction increases in negative direction as seen in Figure 5.3(a). Figure 5.3(b) shows that displacement in the y direction slightly increases, while inherent strain in y direction has small effect on the y displacement. Overall, strains are small in the transversal direction due to the short base length.

At 45° orientation, with increasing the x and y inherent strains magnitude, displacement in x direction increases in negative direction as shown in Figure 5.3(c). Zero value for inherent strain makes calculations difficult, which results the deviating trend in the corresponding curve. Figure 5.3(d) shows, that displacement in the y direction slightly increases with the increasing inherent strain magnitude in x, while inherent strain in y direction has small effect on the y displacement.

At 90° orientation, the specimen's long axis is parallel to the y axis. Figure 5.3(e) shows that displacement in the y direction slightly increases with the increasing inherent strain magnitude in x, while inherent strain in y direction has small effect on the y displacement. With increasing the x and y inherent strains magnitude, displacement in x direction increases in negative direction as shown in figure 3(f). Note that this figure corresponds well with Figure 5.3(a).

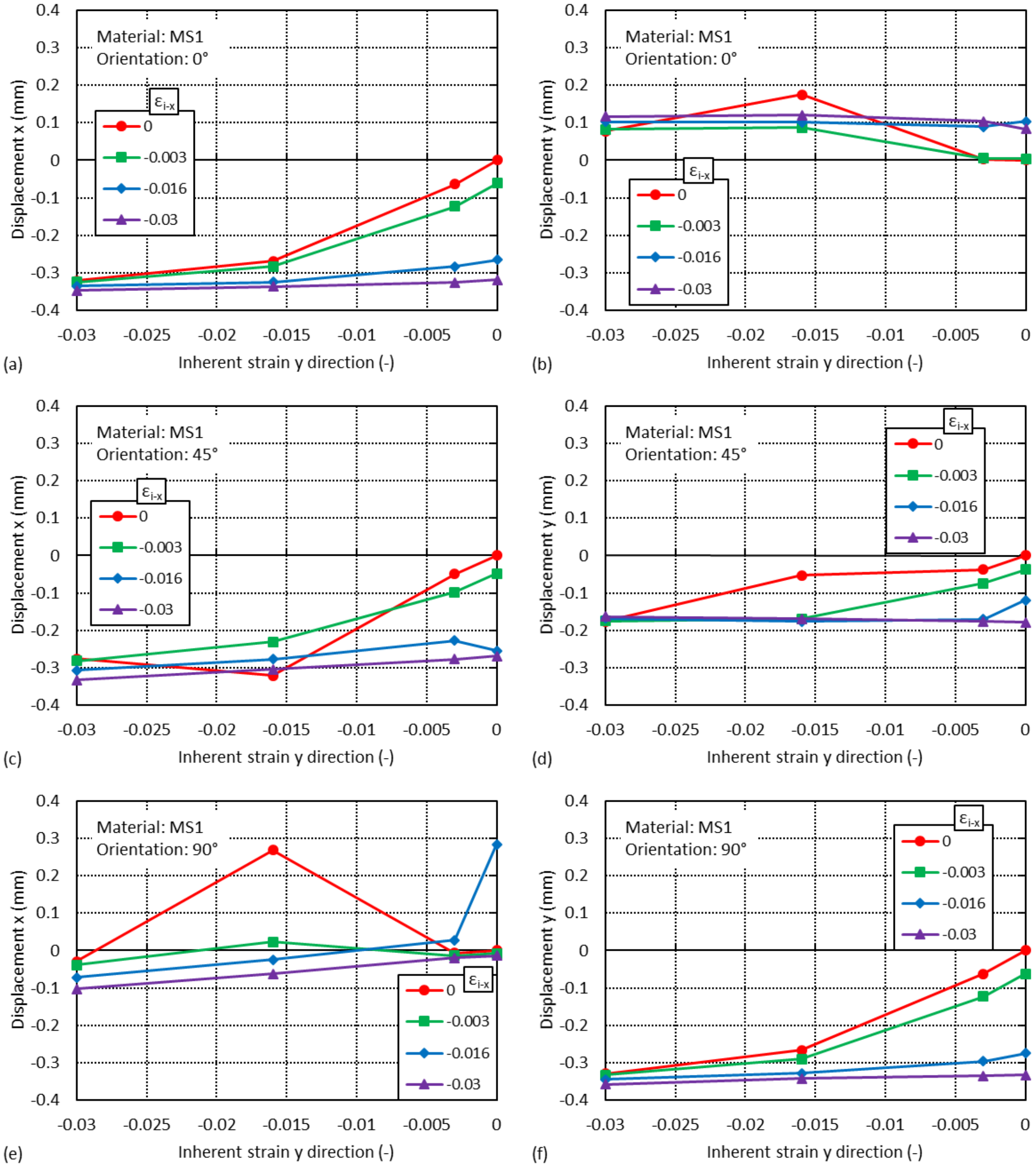

Figure 5.3(a)-(f). Planar displacements (left column: x; right column: y directions) as a function of planar inherent strains (horizontal axis: inherent strain in y direction, parameter for curves: inherent strain for x direction) for MS1 specimens with different orientations (from top to bottom: 0°, 45°, 90°).

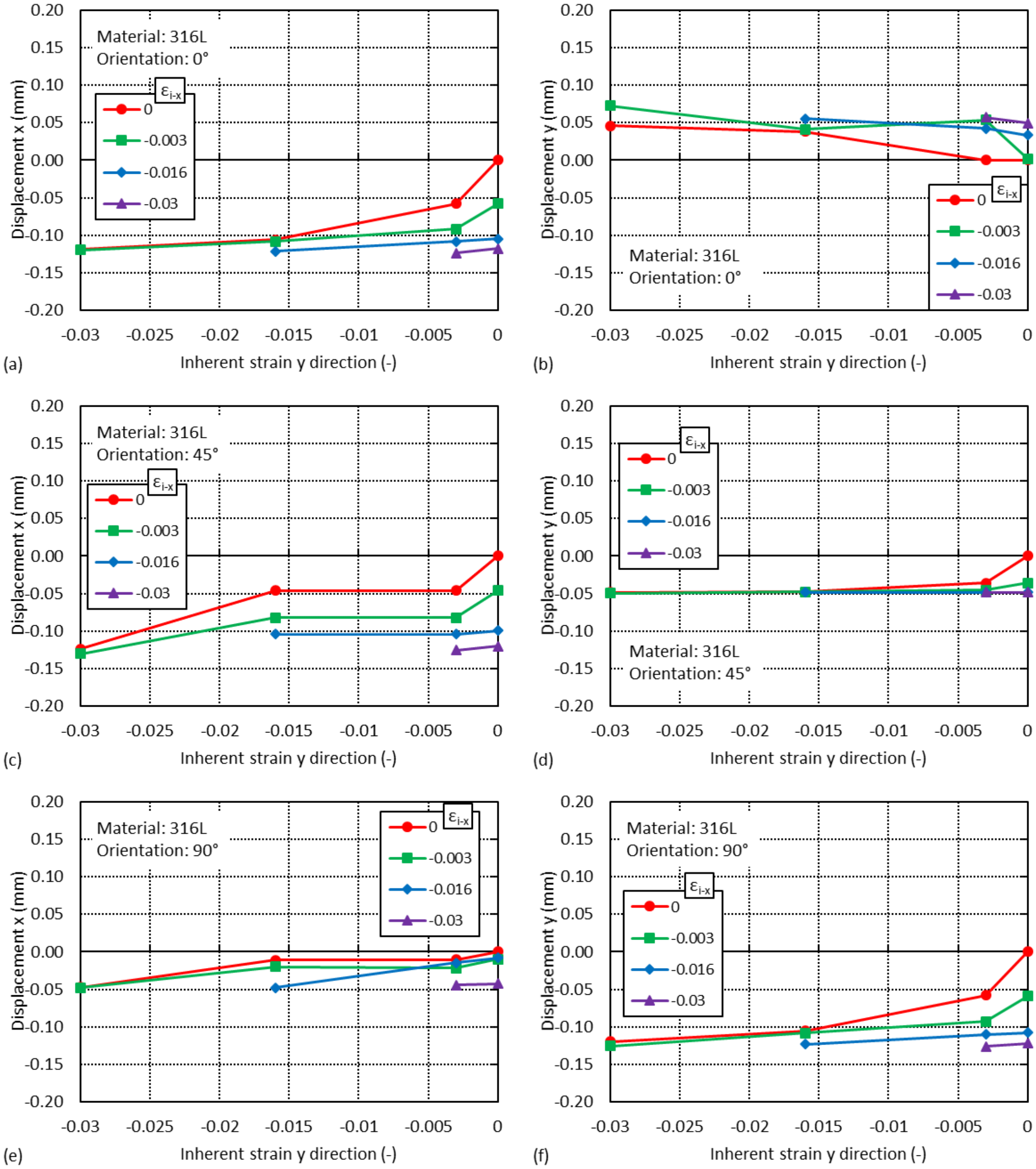

Figure 5.4(a)-(f). Planar displacements (left column: x; right column: y directions) as a function of planar inherent strains (horizontal axis: inherent strain in y direction, parameter for curves: inherent strain for x direction) for 316L specimens with different orientations (from top to bottom: 0°, 45°, 90°).

Effect of orientation for MS1 specimens: at 0° orientation, both planar inherent strain component have the same effect on the x displacements, which converge to the same value. At 45°, the trend is similar, while uncertainty in the displacements are high. At 90°, the effect of the inherent strains are smaller on the x displacements, uncertainty is high at low x inherent strains. For y displacements, the same statements apply for the opposite orientation order.

By comparing the planar displacements with respect to the orientations of the 316L specimens, the following can be found: for 0° orientation, the specimen's long axis is parallel to the x axis; with increasing the x and y inherent strains magnitude, displacement in x direction increases in negative direction as seen in Figure 5.4(a). Figure 5.4(b) shows that displacement in the y direction slightly increases, while inherent strain in y direction has small effect on the y displacement. Simulations failed to complete with high inherent strain pairs.

At 45° orientation, with increasing the x and y inherent strains magnitude, displacement in x direction increases in negative direction as shown in Figure 5.4(c) and curves show a very clear trend. Figure 5.4(d) shows that displacement in the y direction slightly increases with the increasing inherent strain magnitude in x with a very clear trend, while overall the displacement values are small.

At 90° orientation, the specimen's long axis is parallel to the y axis. Figure 5.4(e) shows, that displacement in the y direction slightly increases with the increasing inherent strain magnitude in x, while inherent strain in y direction has small effect on the y displacement. With increasing the x and y inherent strains magnitude, displacement in x direction increases in negative direction as shown in Figure 5.4(f). Note that this figure corresponds well with Figure 5.4(a).

The effect of orientation for 316L specimens is analyzed by the displacements. For x displacement, at 0° orientation both inherent strain components have strong effect, displacements converge to the same value. At 45° orientation, the trend is similar, but the effect is weaker. At 90° orientation, the sensitivity of displacements are smaller, at small inherent strains in x, the uncertainty is large. For y displacements, the same statements apply for the opposite orientation order.

Comparing of material grades with respect to the magnitude of the deformations, for identical inherent strains, displacements are generally higher for MS1 than for 316L material.

This difference is caused by the difference in the strength of the materials, and it is inversely proportional to the strength.

Effect of the geometry of the part is straightforward: larger displacement occurs at larger dimensions, as shown of displacements in the long axial and short transversal dimensions.

5.3 Conclusions

Upon the simulation results of deformation of printed MS1 and 316L specimens with varying the planar inherent strain values, the following conclusions can be drawn: (1) A parameter study of inherent strains prior to the calibration reveals the deformation behavior of the part. (2) The complex deformation behavior of a part is difficult to predict in advance only upon the inherent strains, as it is affected by material and structural nonlinearities, and the gradual gain of new material during the build. (3) Simulations showed, that high strength MS1 material specimen deforms more than the less high strength 316L for the same set of inherent strains. Real inherent strain values may differ for the materials.

5.4 Proposition

Inherent strain approach can largely accelerate simulations of metal additive manufacturing for distortions and warpage. Sensitivity of distortions is decreasing with the increasing inherent strains and smaller yield strength [10].

III Impact of Results

Integration of excimer laser annealing into cleanroom process flows and device fabrications is challenging due to the variations in optical and thermal properties of the targets. An extreme short transient thermal cycle is inherent with surface melt laser treatments with nanosecond pulses, which provide ultimately rapid localized heat treatments with further application possibilities for thermal restricted structures and for ultrashallow junctions. Solutions for fine tuning the thermal budget for rapid thermal annealing of low energy implants with XeCl excimer laser setups have been realized. These results have an impact on designing surface laser heat treatments by precisely tailoring ultimate rapid thermal anneals, especially double laser annealing with overlapping thermal cycles. During the project, extensive cooperation and networking was established with Exico, France and CNR, Sicily; research was continued within a PhD project at the Delft University of Technology.

Along the metallurgical length in continuous casting, particularly in the mushy zone, mechanical properties drastically drop at above the zero deformation temperature and the zero strength temperature due to the presence of liquid phase, moreover these critical temperatures are sensitive for variations of the local chemical compositions. Critical temperatures were determined in the cross section of an as-cast ST52-3 steel strand through hot tensile tests on samples taken from the positions of the columnar grains zone and from the segregated zone located at the centerline of the strand. A significant drop in critical temperatures was found due to segregations in the centerline compared to the columnar zone within the strand. These results have an impact on modeling and analyzing the mechanical behavior of the strand in continuous casting. During the project, extensive cooperation and networking was established with Dunaferr Steel works, Hungary and Bay-ATI, Hungary; a similar topic in semi-solid processing was continued within a PhD research at Óbuda University.

High strain rate extremes occur at special forming technologies as electromagnetic forming, in its frequent industrial application of joining by electromagnetic compression of tubular parts. The goodness of the joints is determined by the strength of the joint, and it is considered excellent if it reaches the strength of the weaker material. Low electromagnetic pressure joining of tubular parts has been demonstrated by using radial and axial grooves to employ interlocking by form fitting, and a computational cost effective modeling was developed. These results have an impact on designing joints. During the project, extensive cooperation and networking was established S-Metalltech Kft. Hungary, and Nordmetall GmbH, Germany.

For pure metals, high strength and performance originated from equal channel angular processing are accompanied with low thermal stability due to the uninhibited driving force for recrystallization by the large stored energy. The applied deformation is determined by the geometry of the extrusion die and the number of passes, nevertheless the microstructural changes and the stored energies are also dependent on the processing routes as well as on the processing temperature. By the elevated temperature single pass ECAP processing of copper, the thermal behavior during the restoration processes of the processed samples was determined. These results have an impact on tailoring material performance within the passes, and spreading the concept of energy based rather than the conventional strain based classification of severe plastic deformations. During the project, extensive cooperation and networking was established with the University of Dunaújváros, Hungary, and the ELTE University, Hungary and the study of the performance on Al alloys is ongoing.

Macro scale simulations of the metal additive printing process are possible on solely a mechanical domain to estimate the deformations within a relatively short computational time by employing the inherent strains, which can be considered as calibration parameters for a specific material quality, machine, and process parameter set. The effect of the magnitude of inherent strain was examined for the simulated deformations of a printed specimen either of MS1 or 316L steel powders. Results showed that the deformation in the printed part might also be strongly influenced by the elastic/plastic mechanical properties of the different steel grades while the same sets of inherent strain values with different magnitude and directional variations are chosen, allowing isotropic and orthotropic behavior. These results have an impact on the planning of metal printing and on the conceptual effect of inherent strains in modeling. During the project, extensive cooperation and networking was established with SME’s in Hungary, and Neumann Faculty of Informatics, Óbuda University, where results were used as an input data for artificial intelligence modeling of the printing process.

IV References

[Balogh et al., 2006] Balogh, L., Gubicza, J., Hellmig, R. J., Estrin, Y., Ungár, T. (2006) Kristallogr. Suppl., 23, 381-386.

[Bean et al., 2019] Bean, G. E., McLouth, T. D., Witkin, D. B., Sitzman, S. D., Adams, P. M., Zaldivar, R. J. (2019) J. Matls. Eng. and Performance, 28, 1942.

[Benchabane et al., 2008] Benchabane, G., Boumerzoug, Z., Tibon, I., Gloriant, T. (2008) Mater Char 59, 1425-1428.

[Deng et al., 2007] Deng, D., Murakawa, H., Liang, W. (2007) Comput. Methods Appl. Mech. Eng., 196, 4613.

[EOS, 2017] EOS material datasheet, 2017, EOS GmbH, www.eos.info

[Gonda et al., 2006] Gonda, V., Liu, S., Scholtes, T. L. M., Nanver, L. K. (2006) in Doping Engineering for Device Fabrication, Proc. Mat. Res. Soc. Symp., 912.

[Gonda et al., 2007] Gonda, V., Slabbekoorn, J., Nanver, L. K. (2007) Proc. IEEE-RTP, 15, 257.

[Gonda, 2008] Gonda, V. (2008) PhD thesis, Delft University of Technology.

[Göbl, 1978] Göbl, N. (1978) PhD thesis, Technical University of Budapest.

[Hegedűs et al., 2013] Hegedűs, Z., Gubicza, J., Kawasaki, M., Chinh, N. Q., Lábár, J. L., Langdon, T. G. (2013) J Mater Sci, 48, 4637–4645.

[Higuera et al., 2011] Higuera, O. F., Calvillo, P. R., Cabrera, J. M. (2011) AIP Conf. Proc. 1353, (2011), 553-558.

[Hill et al., 1995] Hill, M. R., Nelson, D. V. (1995) Proc. Asme PVP1995, 318, 343.

[Kang et al., 2019] Kang, S., Kim, J., Jang, Y., Lee, K. (2019) Appl. Sci., 9, 3848.

[Kim et al., 2015] Kim, T-J., Jang, B-S., Kang, S-W. (2015) Int. J. Nav. Archit. Ocean Eng., 7, 157.

[Langi et al., 2021] Langi, E., Zhao, L. G., Jamshidi, P., Attallah, M. M., Silberschmidt, V. V., Willcock, H., Vogt, F. (2021) J. Matls. Eng. and Performance, 30, 696.

[Liang et al., 2019] Liang, X., Chen, Q., Cheng, L., Hayduke, D., To, A. C. (2019) Comput. Mech., 64, 1719.

[Lorito et al., 2006] Lorito, G., Gonda, V., Liu, S., Scholtes, T. L. M., Schellevis, H., Nanver, L. K. (2006) Proc. MIEL, IEEE, 369-372.

[Lorito et al., 2008] Lorito, G., Gonda, V., Scholtes, T. L. M., Nanver, L. K. (2008) Proc. MIEL, IEEE, 291-294.

[Lu et al., 2019] Lu, Q., Beauchesne, E., Liszka, T. (2019) Int. J. Multiscale Computational Eng., 17, 65.

[Ma et al., 2016] Ma, N., Nakacho, K., Ohta, T., Ogawa, N., Maekawa, A., Huang, H., Murakawa, H. (2016) Proc 35th Int. Conf. Ocean, Offshore and Arctic Eng.

[Mamalis et al., 2005] Mamalis, A.G., Manolakos, D.E., Kladas, A.G., Koumoutsos, A.K. (2005) Journal of Materials Processing Technology, 161, 294–299.

[Molodova et al., 2007] Molodova, X., Gottstein, G., Winning, M., Hellmig, R.J. (2007) Mat. Sci. Eng. A, 460-461, 204-213.

[Rácz et al., 2014] Rácz, P., Göbl, N., Horváth, D., Mamalis A.G. (2014) Materials Science Forum, 792, 115–120.

[Radhamani et al., 2021] Radhamani, A. V., Lau, H. C., Ramakrishna, S. (2021) J. Matls. Eng. and Performance, 30, 3492.

[Sarkar et al., 2012] Sarkar, A., Suwas, S., Goran, D., Fundenberger, J., Toth, L., Grosdidier, T. (2012) Powder Diffraction, 27(3), 194-199.

[Seol et al., 2000] Seol, D. J., Won, Y.M., Oh, K.H., Shin, Y.C., Yim, C.H. (2000) ISIJ Int. Vol. 40, 356.

[Setien et al., 2019] Setien, I., Chiumenti, M., van der Veen, S., San Sebastian, M., Garciandía, F., Echeverría, A. (2019) Computers and Mathematics with Applications, 78, 2282.

[Simufact, 2020] Simufact Additive finite element analysis software, Simufact Engineering GmbH, Germany

[Suzuki et al., 1984] Suzuki, H., Nishimura, S., Nakamura, Y. (1984) Trans. ISIJ Vol. 24, 54.

[Ueda et al., 1993] Ueda, Y., Yuan, M. G. (1993) J. Eng. Matls. and Technology, 115, 417.

[Venturini et al., 2003] Venturini, J., Hernandez, M., Zahorski, D., Kerrien, G., Sarnet, T., Debarre, D., Boulmer, J., Laviron, C., Semeria, M.-N., Camel, D., Santailler, J.-L. (2003) Proc. Mat. Res. Soc. Symp., 765(D7.3), 1-6.

[Weddeling et al., 2011] Weddeling, Ch., Woodward, S. T., Marre, M., Nellensen, J., Psyk, V., Tekkaya, A. E., Tillmann, W. (2011) Journal of Materials Processing Technology, 211, 925-935.

[Wood et al., 1984] Wood, R. F., Jellison, G. E. (1984) Semiconductors and Semimetals, 23, 165.

V Selected Publications

[1] Gonda, V., Venturini, J., Sabatier, C., Van Der Cingel, J., Nanver, L.K.: Thermal budget considerations for excimer laser annealing of implanted dopants (2010) Journal of Optoelectronics and Advanced Materials, 12 (3), pp. 466-469.

[2] Biasotto, C., Gonda, V., Nanver, L.K., Scholtes, T.L.M., Van Der Cingel, J., Vidal, D., Jovanović, V.: Low-complexity full-melt laser-anneal process for fabrication of low-leakage implanted ultrashallow junctions (2011) Journal of Electronic Materials, 40 (11), pp. 2187-2196. DOI: 10.1007/s11664-011-1734-6

[3] Biasotto, C., Jovanović, V., Gonda, V., Van Der Cingel, J., Milosavljević, S., Nanver, L.K.: Integration of laser-annealed junctions in a low-temperature high-k metal-gate MISFET (2009) Proc. ULIS, pp. 181-184. DOI: 10.1109/ULIS.2009.4897566

[4] Nanver, L.K., Schellevis, H., Scholtes, T.L.M., La Spina, L., Lorito, G., Sarubbi, F., Gonda, V., Popadić, M., Buisman, K., De Vreede, L.C.N., Huang, C., Milosavljević, S., Goudena, E.J.G.: Improved RF devices for future adaptive wireless systems using two-sided contacting and AlN cooling (2009) IEEE Journal of Solid-State Circuits, 44 (9), pp. 2322-2338. DOI: 10.1109/JSSC.2009.2023016

[5] Gonda, V., Csepeli, Z., Kardos, I., Verő, B., Csizmadia, J.: Hot ductility variations of ST52-3 continuously cast steel within the cast strand (2010) Materials Science Forum, 659, pp. 13-18. DOI: 10.4028/www.scientific.net/MSF.659.13

[6] Gonda, V., Rácz, P., Horváth, D., Mamalis, A.: Joining of tubular parts by electromagnetic forming: Computational investigations of strength (2014) Materials Science Forum, 792, pp. 194-197. DOI: 10.4028/www.scientific.net/MSF.792.194

[7] Gonda, V.: Thermal behavior of copper processed by ECAP at elevated temperatures (2018) AIP Conference Proceedings, 1960, DOI: 10.1063/1.5034925

[8] Jóni, B., Gonda, V., Verő, B., Ungár, T.: X-ray line profile analysis of equal channel angular pressing processed Cu (2014) IOP Conference Series: Materials Science and Engineering, 63 (1), DOI: 10.1088/1757-899X/63/1/012136

[9] Pázmán, J., Fehér, K., Gonda, V., Verő, B.: Effect of the homogenization and cold deformation on the mechanical performance of Al8006 aluminium alloy (2020) IOP Conference Series: Materials Science and Engineering, 903 (1), DOI: 10.1088/1757-899X/903/1/012039

[10] Gonda, V., Felde, I., Horváth, R., Réger, M.: Inherent strain based estimate of the residual deformations for printed MS1 and 316L parts (2022) IOP Conference Series: Materials Science and Engineering, 1246, 012010, DOI:10.1088/1757-899X/1246/1/012010